'Microbial mortar'-restoration of degraded marble structures with microbially induced carbonate precipitation

James M. Minto [a,*], Qian Tan [b], Rebecca J. Lunn [a], Gráinne El Mountassir [a], Hongxian Guo [b], Xiaohui Cheng [b]

[a] *Department of Civil and Environmental Engineering, University of Strathclyde, Glasgow, UK*
[b] *Department of Civil Engineering, Tsinghua University, Beijing, China*

HIGHLIGHTS

- Microbial mortar can successfully restore degraded marble.
- Reagent transport evolved with each treatment cycle.
- Micro-continuum flow simulation of 3D X-ray data revealed changing flow paths.

ARTICLE INFO

ABSTRACT

To evaluate a restoration strategy for highly degraded marble structures, microbially induced carbonate precipitation (MICP) has been employed to reduce porosity and permeability in a column filled with coarse crushed marble. A 3D X-ray tomography scan revealed the spatial variation in porosity throughout the column and tracer breakthrough curves, recorded at intervals during treatment, enabled derivation of core-scale fluid transport properties and their alteration by precipitating carbonate. Micro-continuum scale flow modelling based on the X-ray data indicated that treatment led to changes in the pore network structure with flow increasingly focused into a smaller number of faster flowing open channels.
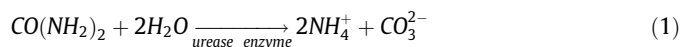
1. Introduction

Since antiquity, architects have focused on the use of durable stone, such as marble and limestone, for the construction of historic monuments. External walls and facades of such monuments are exposed to variable environmental conditions and pollution, which contribute to progressive degradation of the stone. Conventional treatments have shortcomings. Organic treatment materials age rapidly which can result in aggravated weathering [1–3]. Inorganic materials (such as cement mortar) successfully fill cracks within the stone, but the swelling of dissolvable crystalline minerals and their different expansion coefficients can lead to accelerated structural weathering and secondary degradation mechanisms [3,4]. Hence, there is a need to develop novel protection and restoration strategies that maintain the original aesthetics of stone structures.

The phenomenon of microbially induced carbonate precipitation (MICP) is common in the natural environment, occurring in soil and seawater [5]. MICP is the mineralization arising from the metabolic processes of a microorganism. The most commonly studied MICP pathway utilizes the enzymatic action in the growth and reproduction process of certain bacterial strains to hydrolyse urea and generate carbonate ions. The biochemical reactions are as follows:

$$CO(NH_2)_2 + 2H_2O \xrightarrow[urease\ enzyme]{} 2NH_4^+ + CO_3^{2-} \qquad (1)$$

$$Ca^{2+} + cell \rightarrow cell - Ca^{2+} \qquad (2)$$

$$cell - Ca^{2+} + CO_3^{2-} \rightarrow CaCO_3 \downarrow \qquad (3)$$

The resulting calcium carbonate is inorganic (whilst containing residual isolated bacteria) and has excellent adhesion and consolidation properties [6,7]. As such MICP has been investigated as a technique for protecting and restoring historic stone monuments [7–10]. Previous studies can be classified as those relating to (i) *biodeposition* – where the resulting calcium carbonate forms a

surface coating on stone construction materials (Fig. 1a) and (ii) *biocementation* – where the induced calcium carbonate forms a binder material to repair cracks and cavities [11] (Fig. 1b–d).

Le Métayer-Levrel et al. [8] utilized different bacterial species and successfully induced calcium carbonate crystal deposition to form a mineralized layer on the surface of limestone buildings, monuments and sculptures. Rodriguez-Navarro et al. [9] used Myxococcus xanthus to form a mineralized layer on a porous limestone surface. The depth of the coating reached as much as 500 μm without clogging the original pores. De Muynck et al. [10] also investigated MICP for surface coating limestone and showed that the MICP treatment was similar in terms of waterproofing and consolidation to more commonly used ethylsilicates. Li and Qu [12] conducted a series of experiments on marble structures of historic architectural heritage. They found that precipitation had no significant effect on the pore size distribution of the matrix, but resulted in a decrease in porosity, and produced mineral crystals that were strongly attached to the substratum. Zhu et al. [13] utilized both the immersion method and the coating method to produce coatings on sandstone surfaces. The results showed that both methods could form a dense mineralization membrane layer with a thickness of 50–100 μm. Laboratory studies of biodeposition have focused on applying the technique by spraying/painting of stone surfaces with treatment reagents or by total immersion of the stone in the treatment fluids; however the latter is not a practical method for *in-situ* application.

MICP technology can also be used in crack remediation, with previous studies investigating the remediation of cracks in concrete and cement [14–16]. In ground engineering MICP has also been investigated for sealing fractures in sandstone [17], dacite [18] and granite [19,20]. In crack remediation of construction materials a filler material is often introduced. For example Ramachandran et al. [15] filled cracks in cement mortar with sand and bacteria prior to immersion in $CaCl_2$/urea solution. It should be noted that Ramachandran et al. [15] only observed carbonate precipitation close to the surface of the crack; similar observations were also made by Day et al. [16]. Zhong and Islam [19] investigated a range of filler materials/composition for crack sealing in granite and showed that sand (80%) and silica fume (20%) resulted in the highest compressive strength. The introduction of a filler requires that cavities are pre-packed with filler particles prior to the application of treatment reagents (Fig. 1b), this limits treatment to surface cracks only. Alternatively filler particles can be introduced simultaneously with the treatment reagents (in the form of a paste) (Fig. 1c), this technique has been trialled by Le Métayer-Levrel et al. [8] and Orial et al. [21]. Both of these techniques help to reduce crack porosity thus requiring a smaller volume of calcium carbonate to be precipitated to change the bulk properties of permeability or strength. However the depth of cracks which can be treated in this manner is limited to several cms or less.

Finally MICP may also be applied to restore cracks, which contain existing stone grains that have detached during progressive

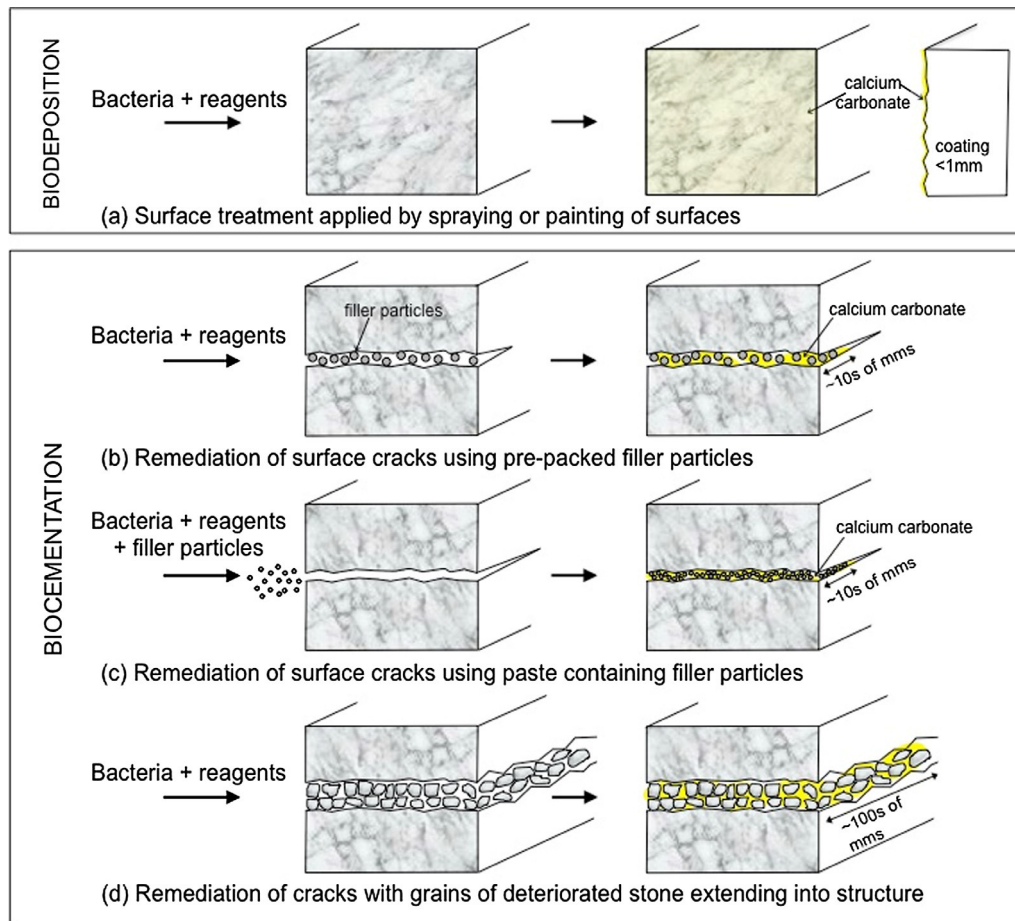**Fig. 1.** Applications of MICP in restoration of stone monuments: (a) Biodeposition – surface treatment applied via spraying or painting of surfaces and Biocementation: (b) Remediation of surface cracks using pre-packed filler particles, (c) Remediation of surface cracks using paste with filler particles and (d) Remediation of cracks with grains of deteriorated stone extending into structure.

weathering and ageing (Fig. 1d). Previous research by the authors [22], demonstrated successful sealing of a crack filled with fine-grained marble powder (0.1–0.2 mm), creating in effect a 'microbial mortar'. In this case, the extent of treatment is not limited by the ability to transport filler materials, but rather on the transport of the bacteria and reagents. In order to limit the number of injection points (and hence cost and invasiveness of the technique) the deployment of MICP to stone structures should seek to maximize the penetration of treatment fluids and subsequent carbonate precipitation. Controlling and predicting the extent of treatment in stone monuments requires detailed modelling of the process; a critical component of this is a detailed understanding of reagent transport and how it evolves as a result of mineralization.

In this paper we investigate the ability of MICP to seal cracks containing larger marble grains (0.5–1.4 mm), binding them together with microbial mortar, and determine the uniformity of treatment. This was achieved by filling a column with marble grains, precipitating $CaCO_3$ throughout the column via MICP and evaluating spatial $CaCO_3$ distribution using X-ray computed tomography (X-CT). Tracer tests and numerical modelling of the porous media were carried out to better understand changes in reagent transport due to $CaCO_3$ precipitation. The implications this may have for MICP injection strategies for stone restoration are considered.

2. Marble column experiment

2.1. Experimental methods

2.1.1. Materials

The ureolytically active bacterial strain used in this study was *Sporosarcina pasteurii* (strain DSM-33). *S. pasteurii* is a Gram-positive bacterium commonly found in soil and its use for MICP has been extensively studied. The bacteria were cultured on brain heart infusion broth (37 g/L, sterilized by autoclave) with urea (20 g/L, syringe filter sterilized) added after autoclaving. Cultures were incubated for 24 h in a shaker-incubator set to 30 °C and 100 rpm. Optical density of the resulting bacterial suspension was measured on a UV-Vis spectrophotometer at a wavelength of 600 nm. This measurement, hereafter referred to as OD_{600}, serves to quantify the amount of bacteria in the suspension.

The urease activity was measured using the conductivity method [23] in which 3 mL of bacterial suspension was added to 27 mL of 1.11 M urea solution. Conductivity change over a five minute period was recorded as non-ionic urea was hydrolyzed to ionic ammonium. The rate of conductivity change was converted from mS/cm/min to mM urea hydrolyzed/min using the conversion factor of 10.62 [20], then normalized by OD_{600} to yield ureolytic activity with units mM urea/min/OD.

The cementing solution was prepared by dissolving 0.4 M urea and 0.4 M $CaCl_2$ in de-ionised water, then adjusting pH to 6.5 with hydrochloric acid so as to delay the onset of precipitation and reduce blockage of the injection point [24].

The marble grains used in the test were created by crushing marble gravel, resulting in the grading curve presented in Fig. 2. The mean particle size of the marble grains was 0.91 mm.

2.1.2. Treatment strategy and permeability measurement

The experimental setup consisted of three main parts: a column, a pump and a piezometer for pressure measurement (Fig. 3). The column consisted of a cylindrical polycarbonate tube and two metal caps with watertight seals, as well as an inlet and outlet (each with metal plates that support the media and distribute flow) at the top and bottom respectively. The inner diameter and length of the container are 76 mm and 230 mm. A peristaltic pump controlled injection at a constant flow rate.

The column was filled with 1904.3 g of washed and dried marble grains with a particle size of 0.5–1.4 mm; the resultant porosity of the column was 32.4% with a liquid pore volume of 338 mL. In this experiment, six batches of MICP grouting were performed with one batch injected per day, as summarised in Table 1. Each batch consisted of five alternating injections of 60 mL bacteria followed by 400 mL cementing solution with no break in between. Total batch volumes were 300 mL bacteria and 2000 mL cementing solution per day with an injection duration of 2.74 h (flow rate = 14 mL/min). For the remainder of the day there was no flow within the column, with the exception of tracer injections (Section 2.1.3) and permeability measurements, the latter of which were performed daily with a de-ionised water injection immediately prior to the MICP batch injection.

This strategy of repeated short pulses of bacteria followed by cementing solution and subsequent periods of no flow was adopted as it promotes mixing of bacteria and cementing solution within the porous media, enhancing bacterial
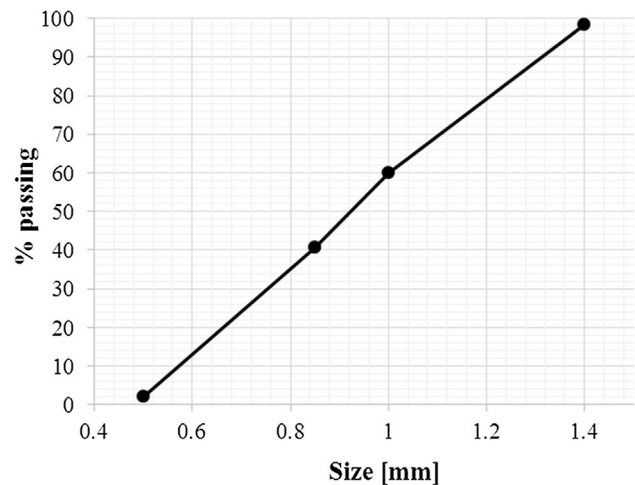
Fig. 2. The grading curve of the crushed marble grains.
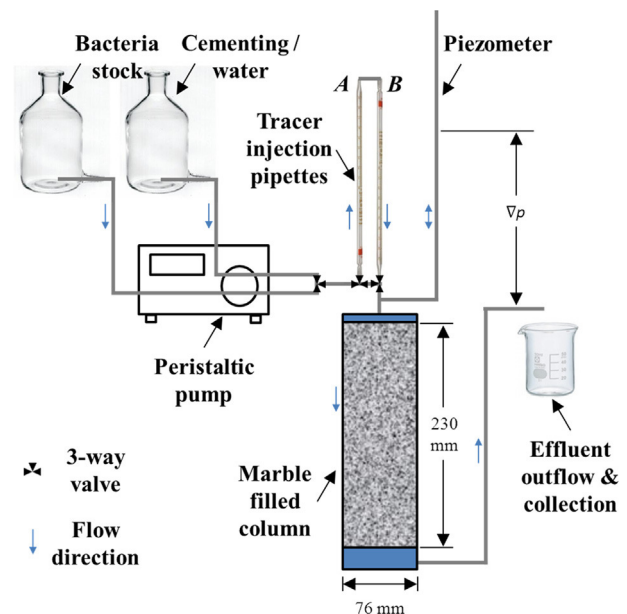
Fig. 3. Schematic of experimental apparatus for injecting bacteria, cementing solution, tracer, and water into the marble filled column. Pressure drop across the column was measured with a piezometer. Tracer volume was precisely controlled using two graduated pipettes connected in series: pipette *B* was pre-filled with tracer, pipette *A* was initially empty but was filled with water via the peristaltic pump displacing the tracer in *B* and injecting it into the column at a constant rate. 3-way valves were used to switch between bacteria, cementing solution, tracer, and water injections.

attachment to surfaces and $CaCO_3$ precipitation within the column. Cheng and Cord-Ruwisch [25,26] employed a similar strategy finding that four pulses precipitated more $CaCO_3$ than two pulses, but that six pulses led to less homogeneous treatment than four, hence, in this experiment, five pulses were chosen so as to maximise homogeneous precipitation. The volume of bacteria in each batch was chosen so as to approximately equal one pore volume whilst the volume of cementing solution was chosen to be greatly in excess so that urea and calcium did not become limiting factors even at the column outlet. The flow rate of 14 mL/min equals a Darcy flux of 18.5 cm/h and is relatively high compared to many previous small scale MICP experiments, but is within the range used in larger scale MICP experiments [26–28] and was chosen with the aim of increasing homogeneity of bacterial attachment throughout the column.

The pressure difference across the sample was recorded at the beginning of the experiment and after consecutive grout batches. Permeability (k) of the marble filled column was calculated over time using Darcy's law, Eq. (4), with pressure from inlet and outlet water elevation measurements made during the injection of de-ionised water that preceded each daily batch injection.

Table 1
Detail of MICP treatment for each batch.

Grout batch	Flow rate [mL/min]	Volume of fluids		Bacteria activity [mM urea/min/OD]	OD_{600}	Remarks
		Bacteria and broth [mL]	Cementation solution [mL]			
1	14	300	2000	4.29	1.732	
2	14	300	2000	4.44	1.532	
3	14	300	2000	3.77	1.636	
4	14	300	2000	4.22	1.812	5 mm at inlet removed
5	14	300	2000	3.83	1.498	
6	14	300	2000	4.61	1.522	

$$k = \frac{Q \mu l}{A p} \qquad (4)$$

where Q = volumetric flow rate [m^3/s], A = cross-sectional area [m^2] and ∇p = pressure drop [Pa].

Before each permeability measurement, the metal inlet cap of the column was removed for inspection and unblocking (if necessary) to ensure an accurate permeability measurement. After the fourth batch of grouting was complete, 5 mm of marble grains were removed from the inlet surface as it appeared to have become blocked.

2.1.3. Tracer transport & bulk flow properties

Fluid transport properties and the porosity of the grouted marble pack were estimated by the use of tracer tests at the beginning of the experiment, after the fourth MICP batch and after completion of grouting. Calcium chloride was used as a conservative tracer. Prior to the start of the test, de-ionised water was injected into the vessel to rinse out any residual electrolyte. After half an hour of flushing, the discharged liquid was collected and tested to ensure conductivity had reached a stable background of less than 200 µm/cm. During each tracer test, 12 mL of tracer was injected into the vessel, followed by injection of de-ionised water, both at a flow rate of 14 mL/min.

During the tracer test, the liquid discharged from the outlet was collected at regular time intervals and the electrical conductivity of the effluent was measured.

CXTFIT/EXCEL [29] was used to estimate solute transport parameters from the tracer tests. Parameter optimization was performed through non-linear least-squares fitting of the tracer breakthrough curves with the convection-dispersion equation. It was assumed that the tracer was conservative and non-reactive in the marble pack/CaCO$_3$ media, and that any non-equilibrium in effluent breakthrough curves was the result of physical processes; namely the mass transfer between mobile and immobile liquid regions within the model.

The two-region (mobile and immobile) non-equilibrium convection-dispersion equation is presented in dimensionless form [30] as follows:

$$\beta \frac{\partial C_m}{\partial T} = \frac{1}{P} \frac{\partial^2 C_m}{\partial L^2} - \frac{\partial C_m}{\partial L} - \omega(C_m - C_{im}) \qquad (5)$$

$$(1 - \beta) \frac{\partial C_{im}}{\partial T} = \omega(C_m - C_{im}) \qquad (6)$$

with Eq. (5) accounting for convective-dispersive solute transport confined to the mobile water phase and Eq. (6) accounting for the first-order diffusion controlled solute transport between mobile and immobile regions. In Eqs. (5) and (6), C = reduced aqueous tracer concentration with subscripts m and im to denote mobile and immobile regions, L = dimensionless distance, T = dimensionless time (i.e. pore volumes), P = Peclet number, β = mobile water fraction, ω = dimensionless mass transfer coefficient. Dispersivity (λ, with units of cm) was calculated from the Peclet number and column length (l, cm) in Eq. (7), whilst the dispersion coefficient (D, cm^2/s) was calculated from Equation (8) with U_s = superficial (Darcy) velocity [m/s]:

$$\lambda = l/P \qquad (7)$$

$$D = \frac{l U_s}{P} \qquad (8)$$

Fitting parameters for the optimization process were dispersivity (via Peclet number), mobile water fraction, and the dimensionless mass transfer coefficient. For the 4× and 6× MICP breakthrough curves, porosity was used as an additional fitting parameter to account for the reduction in pore volume due to CaCO$_3$ precipitation. Mobile water volume was calculated as the product of porosity, mobile water fraction, and total column volume.

A comparison with the equilibrium CDE was made by fixing β at 1 (no immobile region) and ω at 0 (no mass transfer) to determine if the two-region non-equilibrium model was required, or if the equilibrium CDE could provide an adequate fit by including the effect of immobile regions within the porosity fitting parameter.

2.1.4. X-CT scan acquisition

After completion of the MICP and tracer injection, the column was flushed with de-ionised water, drained, then dried by a forced flow of dry air until it reached a constant weight (after approximately three days) and all moisture was removed. The dried sample was scanned with a Nikon Metrology X-ray micro CT system with 225 kV X-ray source and a 3D volume reconstructed using Nikon XTekCT software version 4.3.4.

To maximise spatial image resolution of the tall column, four scans along the column length were made, each with a 13% overlap. The four scans were combined into a single data set consisting of 10.35 billion voxels covering the entire porous media within the column with a resolution of 50.00 µm.

Scan parameters were 3141 projections (per scan, angular step 0.1146 degrees), 190 kV, 118 µA, 2829 milli-second exposure, with 2 mm copper filtration to minimise beam hardening artefacts.

As stated in Section 2.2, the last 80 mm of the column was poorly cemented. It was assumed that minimal CaCO$_3$ had been precipitated in this outlet region hence the average porosity should be equal to the column average porosity pre-MICP. To perform binary segmentation, a global threshold was applied to the outlet region X-ray attenuation values: all those below the threshold were set as pore space (value of 1) whilst all those above were set as solid (value 0). The outlet region average value therefore equals the average porosity. The global threshold value was varied until X-CT porosity matched the 32.4% experimentally measured porosity. This global threshold was then applied to the entire X-CT dataset to give the porosity distribution throughout the column.

2.2. Experimental results

Visual observations during the course of the experiment confirmed an increased mass of CaCO$_3$ precipitation with each batch of grout treatment. A minimal amount of precipitate was also observed where fluids mixed in the effluent container.

After all six batches of grout had been injected (and after the X-CT scan), the column top and bottom cap were removed. Preliminary inspection of the marble grains showed that the inlet was well cemented whilst towards the outlet the marble grains were loose and similar to the initial state. Gentle excavation of the material showed that cementation ended at around 30 mm from the base. At around 80 mm from the base, the marble grains were sufficiently solid as to resist scraping with a spatula (Fig. 4).

2.2.1. Permeability

Fig. 5 shows the sample permeability evolving with increasing MICP batches; in general, a gradual permeability decrease was observed with increasing numbers of treatment batches. Despite variation in total ureolytic activity (ureolytic activity multiplied by OD_{600}) from +13% to −16% of the mean for all six batches, there appears to be no clear correlation between activity and permeability change. After four batches were injected, the first 5 mm of cemented marble at the inlet was removed. This ensured that the bacteria and cementation solutions could continue to penetrate easily into the column and accounts for the small jump in permeability observed in Fig. 5.

After grouting was complete, 38.1 mm diameter cores were taken for further testing. The marble grains were well enough cemented at the inlet to necessitate coring with a diamond-coated core barrel, however the vibration of the core barrel was significant, causing the core to disaggregate into three sections (Fig. 6). The dimensions, their location along the sample and the mass of each section are shown in Table 2. The marble pack beyond 65 mm from the inlet was not well enough cemented to core.

Only core sample B was long enough for measurement of permeability. Permeability was calculated from Eq. (4) by mounting the sample in a high pressure Hassler-type core holder, applying a radial confining pressure of 300 kPa greater than the injection pressure, injecting water at a constant rate, and measuring pressure drop across the core. Permeability was determined to be 7.16×10^{-14} m^2, significantly less than that of the whole sample, thus confirming that permeability decreases (and cementation increases) towards the inlet, an observation consistent with the X-CT results of Section 2.2.3.
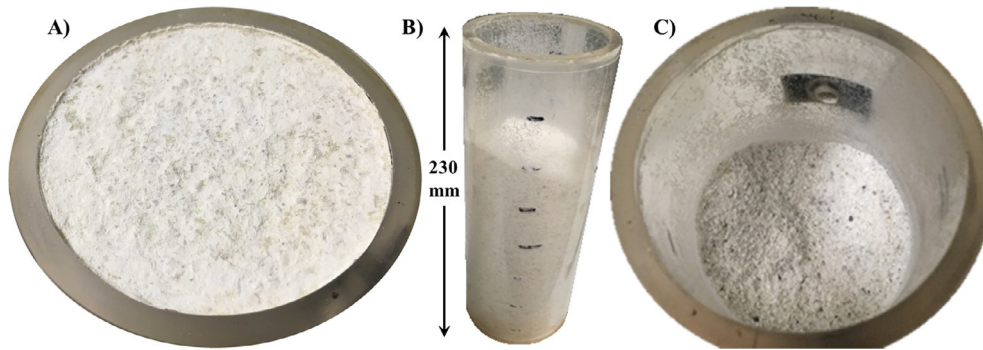
Fig. 4. Cemented marble grains after 6 MICP injection batches: A) the inlet surface, B & C) the inverted column after removal of uncemented and weakly cemented sand near the outlet.
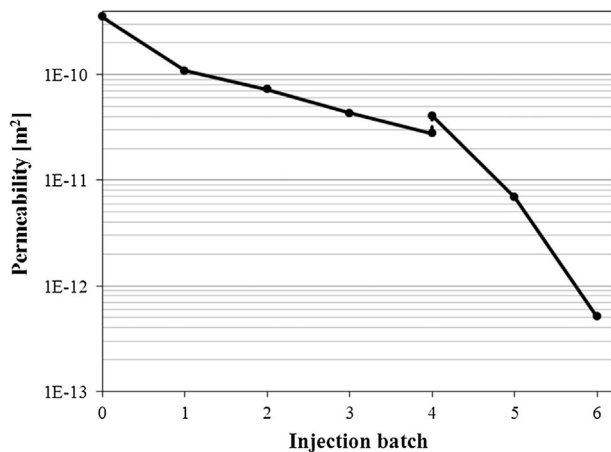

Fig. 5. The variation of column average permeability.

Fig. 6. Core samples (A, B, C from top to bottom) and residual sample.

2.2.2. Tracer breakthrough curves

Fig. 7 shows the CaCl$_2$ breakthrough curve (i.e. the electrical conductivity of the fluid at the outlet) for each of the three tracer tests (markers on Fig. 7). As the number of MICP grout batches increases (Fig. 7), the time to reach peak concentration at the outlet reduces. Tracer recovery for batches 0, 4 and 6 were 102.9%, 107.2%, and 88.3%; this was within the experimental error in terms of injected tracer volume and effluent sampling frequency, hence the CaCl$_2$ can be regarded as a conservative tracer in this system. The breakthrough data were fitted with the equilibrium CDE model (Fig. 7A) and the two-region non-equilibrium CDE model (Fig. 7B). Breakthrough curve fitting with the equilibrium CDE model was poor (Fig. 7A) and resulted in an initial porosity estimate of 0.312. The two-region model (Fig. 7B) shows an excellent fit to the data; the accompanying best-fit model parameters are given in Table 3.

Between batches 0 and 4, dispersivity increases whilst mobile water fraction decreases. The change in porosity is small, but the reduction in mobile volume is significant. This indicates an increase in mixing due to more tortuous fluid flow paths, and the formation of additional stagnant zones. The decrease in time to tracer breakthrough (Fig. 7) is a result of the 9% decrease in the volume of mobile fluid regions in the sample.

From batches 4 to 6 the changes to dispersivity, mobile water fraction and mass transfer coefficient are within the error of one standard deviation and so no conclusions can be drawn. The reduction in porosity and mobile fluid volume, however, are significant. The further decrease in time to tracer breakthrough (Fig. 7) is a result of these reductions in porosity and mobile water volume, not due to a change in dispersivity or mass transfer coefficient since the shape of the breakthrough curves at 4 and 6 MICP batches are nearly identical with only an offset in the x-axis.

If it were assumed that porosity reduction was due to CaCO$_3$ precipitation alone, the volume of CaCO$_3$ precipitated can be estimated as 5.36 mL between batches 0 and 4, with a further 39.39 mL precipitated between batches 4 and 6. This is not thought to represent the actual volume of precipitate, as discussed in Section 4.1.

2.2.3. CT scan results

Fig. 8 shows X-ray attenuation from the four CT scans combined into a single volume, and slice averaged attenuation in which the 3D dataset has been 'sliced' perpendicular to the direction of flow and averaged across that slice. The first 2 mm show low slice average attenuation as the surface of the marble was not level

hence some air is included. Attenuation values at the column outlet were affected by the low density support on which the column rested whilst in the CT scanner. This effect was determined to be noticeable from 217.74 mm onwards and so this region has been excluded from further analysis. X-CT derived bulk porosity was 27.51% within the region of analysis, which is in close agreement to the tracer derived post-MICP bulk porosity of 28.1%.

Slice average porosities show greatest reduction in porosity close to the inlet with a minimum porosity of 7.2% at 4.5 mm. Porosity increases along the direction of flow until the pre-MICP porosity is reached at approximately 150 mm from the inlet. Fig. 9A shows the slice averaged porosity from inlet to outlet, illustrating that the slice averaged porosities can be fitted with a power law equation.

Reducing the CT attenuation data by a factor of ten through linear averaging (i.e. averaging $10 \times 10 \times 10$ adjacent voxels to form a single voxel, applied prior to the global threshold) reduces the dataset from 10.35 billion voxels to a more manageable 10.35 million voxels (shown in Fig. 9B). Porosity varies between 0 and 1 and this dataset is suitable for micro-continuum scale numerical flow modelling, as described in Section 3.

3. Sub-column scale flow modelling

The results of the two-region convection dispersion modelling (Fig. 7a) show that post-MICP treatment tracer transport cannot be well modelled with a single region convection dispersion model. By contrast, post-treatment breakthrough curves are well modelled using a two-region mobile-immobile model in which the fraction of immobile water increases with increasing cycles of MICP. Both the single region model and the mobile-immobile region model assume a single value for porosity throughout the whole column. However, the X-CT data (Fig. 9) indicates that post-MICP, porosity values are *not* uniform throughout the full

Table 2
Details of core samples.

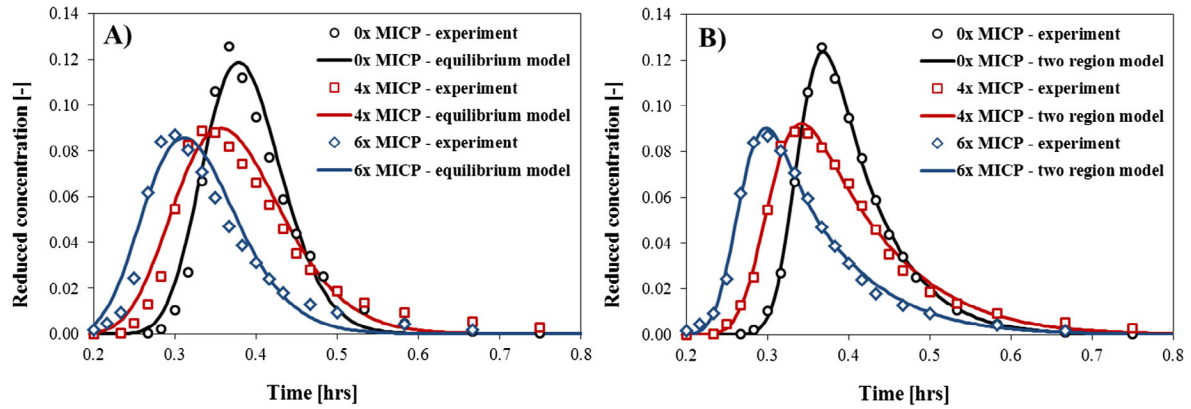| Sample	Mean diameter (mm)	Length (mm)	Mass (g)	Distance from inlet (mm)
A	35.8	15.2	24.94	0–15.2
B	35.6	26.3	48.71	15.2–41.3
C	30.1	23.4	29.74	41.3–64.7

Fig. 7. A) Tracer breakthrough curves measured at the column outlet with the equilibrium CDE model fitted, B) and an improved fit with the two-region non-equilibrium CDE. Reduced concentration measured as effluent conductivity divided by the conductivity of the injected tracer.

Table 3
Fitting parameters (λ, β, ω, ε) from the two-region non-equilibrium model and associated standard deviations. Mobile volume was calculated as the product of β, ε and total column volume. *Porosity from the equilibrium CDE model is shown for reference.

	MICP batches					
	0		4		6	
Dispersivity, λ (cm)	0.070	±0.004	0.127	±0.017	0.122	±0.014
Mobile water fraction, β (−)	0.891	±0.004	0.827	±0.012	0.831	±0.009
Mass trans. coef., ω (−)	1.228	±0.119	1.445	±0.231	1.236	±0.159
Porosity, ε (−)	0.324	–	0.319	±0.002	0.281	±0.002
Mobile volume (mL)	301.14	–	275.29	±2.276	243.67	±2.165
Porosity from equilibrium CDE (−)*	0.312	±0.002	0.302	±0.003	0.263	±0.003

column and that, in fact, porosity decreases toward the inlet. Further the modelled increase in the fraction of immobile water post MICP, accompanied by the decrease in total porosity, implies increased fluid flow channelling within the core, especially at the inlet. To validate this interpretation, sub-column scale finite volume modelling is carried out to relate the changes in flow properties to the pore-scale changes observed at the inlet in the X-CT data, brought about by $CaCO_3$ precipitation. The finite volume software used was OpenFOAM with a custom solver to model flow in a porous media.

3.1. Micro-continuum modelling methodology

At a micro-scale, fluid flow within a porous media can be solved using the Navier-Stokes equations of continuity [Eq. (9)] and momentum [Equation (10)] modified by the addition of a Darcy term for resistance of the porous media and a Brinkman term to account for the dissipative viscous force [31], a force that only becomes significant at higher flow rates. Eqs. (9) and (10) are presented for an incompressible fluid neglecting gravity:

$$\nabla . U_s = 0 \tag{9}$$

$$\frac{\partial U_s}{\partial t} + \nabla . U_s U_s = -\varepsilon \nabla p - \frac{v\varepsilon}{k} U_s + v^2 U_s \tag{10}$$

where t = time [s], ε = porosity [−], p = pressure [Pa], v = kinematic viscosity[m^2/s], and k = permeability [m^2].

The standard OpenFOAM solver named pisoFoam was adapted to include the Darcy and Brinkman terms to account for flow through porous media, with porosity and permeability derived from the X-CT data. This solver utilises the Pressure-Implicit with Splitting of Operators (PISO) algorithm to iteratively solve the Navier-Stokes equations.

X-CT data, processed in the FIJI version of ImageJ [32], was written in OpenFOAM format as a spatially varying scalar field with a custom ImageJ script. The X-CT attenuation was assumed to equal the average density of material contained in each voxel, and, as the sample consisted of only two materials (air filled pores and $CaCO_3$, assuming the marble had the same density as the microbially induced calcite), attenuation can be linearly scaled (between limits) to give the porosity of each voxel with a high attenuation equal to a low porosity. These limits were determined using the attenuation number from areas of the scan that were entirely solid (such as large marble grains) and entirely pore (such as air bubbles).

$$\varepsilon_i = \begin{cases} \varepsilon_L & \text{when } CT_i \geqslant CT_U \\ \frac{(\varepsilon_L - \varepsilon_U)(CT_i - CT_L)}{(CT_U - CT_L)} + \varepsilon_U & \text{when } CT_L \leqslant CT_i \leqslant CT_U \\ \varepsilon_U & \text{when } CT_i \leqslant CT_L \end{cases} \tag{11}$$

where CT_i = X-CT attenuation in a given voxel [m^{-1}], CT_U = upper attenuation limit, CT_L = lower attenuation limit, ε_i = porosity in a given voxel [−], ε_U = upper porosity limit, and ε_L = lower porosity limit.
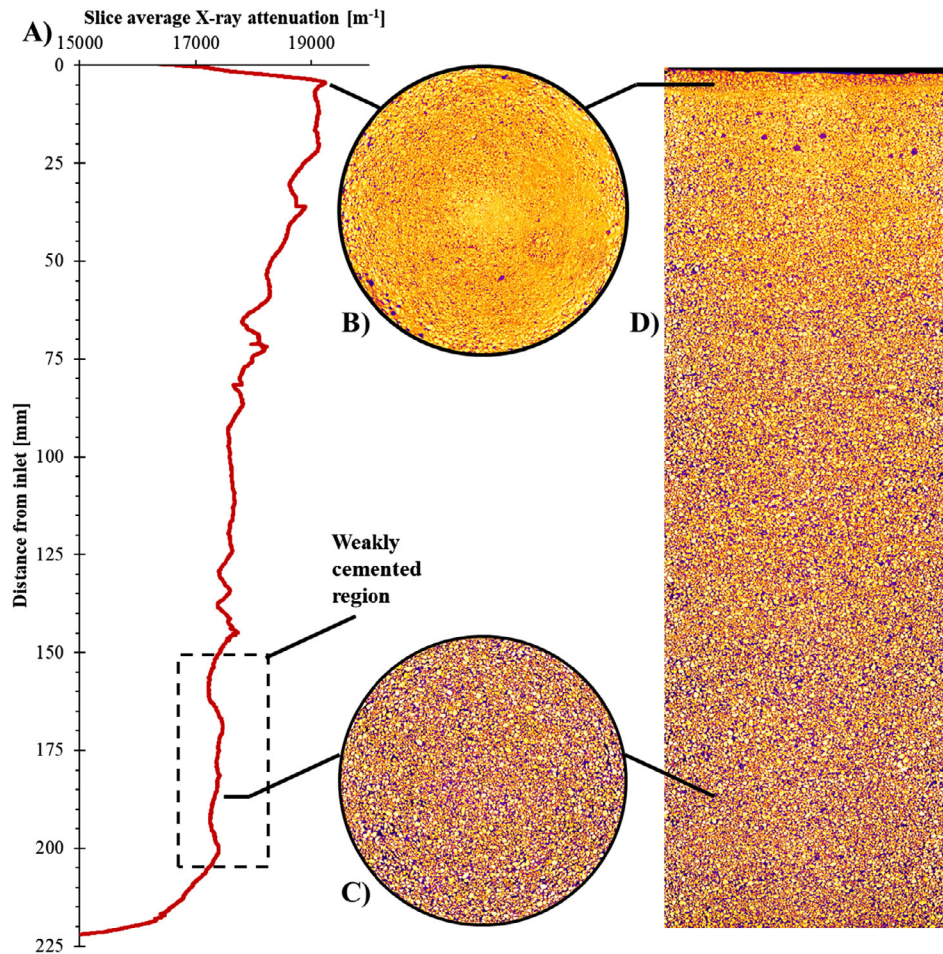
Fig. 8. Composite of four X-ray CT scans showing X-ray attenuation with a resolution of 50 μm. Warm colours (yellow to white) indicate high attenuation from solid material such as quartz sand and $CaCO_3$. Cool colours (purple to black) indicate low attenuation such as air filled pore space. A) Slice averaged X-ray attenuation with extent of weakly cemented region highlighted. Slices taken perpendicular to the direction of flow. B) Attenuation in slice 4.5 mm from inlet with maximum average attenuation. C) Attenuation in slice 192.5 mm from the inlet which is representative of the entire weakly cemented region. D) Attenuation in a vertical profile through centre of the column. (For interpretation of the references to colour in this figure legend, the reader is referred to the web version of this article.)

Permeability was inferred from porosity with the widely-used Kozeny-Carman relationship:

$$k_i = k_0 \frac{\varepsilon_i^3}{(1 - \varepsilon_i)^2} \tag{12}$$

where k_i = permeability in a given voxel [m²] whilst k_0 = base permeability [m²], used as a fitting parameter. It should be noted that Kozeny-Carman relationships can be subject to error when predicting the permeability distributions in rock cores [33,34], however no other method is available.

The base permeability was calibrated by varying k_0 until the average inlet pressure in the model was equal to the experimentally measured inlet pressure, assuming that $\varepsilon_U = 1$ and $\varepsilon_L = 1 \times 10^{-6}$.

3.2. Micro-continuum modelling results

Porosity throughout the column after MICP is shown in Fig. 10A and velocity is shown in Fig. 10B: it is clear that fluid velocity is considerably less uniform near the inlet where $CaCO_3$ precipitation occurred. Channelling of flow is apparent with some high velocity flow paths separated by regions of no (or very low) flow. Flow paths (derived from the velocity vector field) are shown in Fig. 10C; these illustrate that flow follows the pressure gradient from

high (inlet) to low (outlet) with slight deviations where porosity is high (red) and porous resistance therefore lower. Fig. 10D compares the pore velocity with histograms of the first and last 30 mm of the modelled domain, representative of post- and pre-MICP states respectively, and boxplots to capture changes at the extremes (whiskers extend from 0.5 to 99.5%). There is a clear change in the shape of the velocity distribution.

4. Discussion

4.1. Flow transport properties

The CXTFIT/EXCEL two-region non-equilibrium transport model is an excellent fit to the experimental data both before and after $CaCO_3$ precipitation (Fig. 7B). Analysis of the X-CT data shows that porosity varies with distance from the inlet, and that a conceptual model of fluid flow becoming focussed into a gradually decreasing number of discrete higher velocity channels, is valid.

The estimate of 39.39 mL of porosity reduction between MICP batches 4 and 6 (Section 2.2.2) is approximately 7.5 times the porosity reduction between batches 0 and 4 and cannot be attributed to $CaCO3$ precipitation alone. Porosity reduction is most likely due to closing off pore throats and disconnecting large pore bodies/networks from the flow channel rather than completely filling the pore space with $CaCO_3$, as illustrated in Fig. 11.
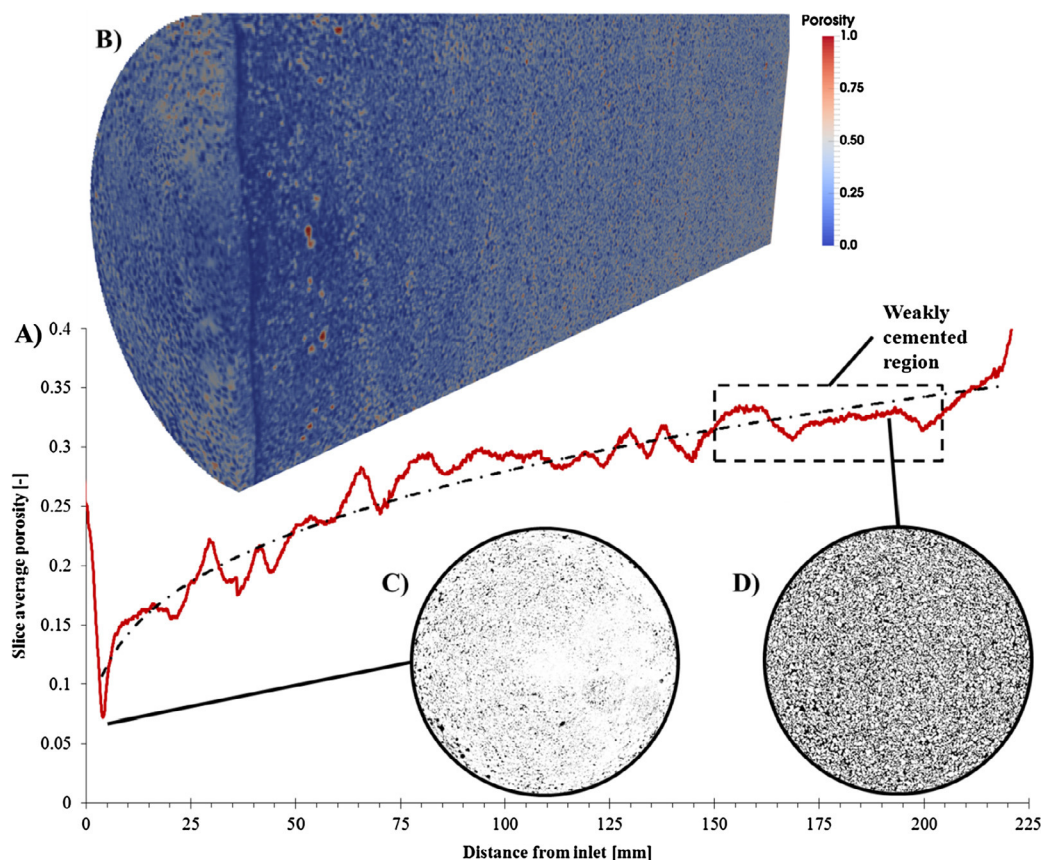
Fig. 9. A) Slice averaged porosity from inlet to outlet calculated after applying global threshold to entire data set and matching average porosity in weakly cemented region to the pre-MICP experimentally measured bulk porosity. B) Cut through 3D representation of porosity after reducing by a factor of ten (voxel resolution now 500 microns). C) & D) porosity in slices at 4.5 and 192.5 mm at 50 μm resolution.

The similarity in CXTFIT/EXCEL transport parameters between batches 4 and 6, which existed despite continued $CaCO_3$ precipitation between these batches, supports previous observations of a feedback mechanism between $CaCO_3$ precipitation and transport of MICP re-agents. This feedback results in the formation of self-organising stable channels similar to those observed in El Mountassir et al. [35] which formed when the fluid velocity exceeded the threshold required to maintain bacterial attachment. Above this threshold, shear forces at the fluid/surface boundary were presumed to prevent bacteria attaching to the surface. Minto et al. [20] found that for MICP precipitation within a large-scale rock fracture, this threshold lies somewhere in the vicinity of 0.55–2 mm/s. From Fig. 10D we see that at the outlet (representative of the marble grains before MICP grouting), interstitial velocity is above 0.55 mm/s for 2.49% of the region (by volume) and above 2 mm/s for only 0.01%. However, at the inlet (where $CaCO_3$ precipitation was greatest), interstitial velocity is above 0.55 mm/s for 25.87% and above 2 mm/s for 0.98%: there is a clear shift from flow being relatively evenly distributed throughout the marble pack to flow becoming concentrated in high velocity channels/preferential flow paths.

Whilst these observations of fluid flow becoming focussed into a gradually decreasing number of discrete higher velocity channels are only for a single column experiment, they are consistent with the MICP fracture sealing experiments of El Mountassir et al. [35]. Attachment in porous media differs from that in fractures, primarily due to the increased likelihood of straining of bacterial cells in pore throats, and wedging into grain contacts. Nevertheless, it is likely that a similar relationship between flow velocity and bacterial attachment exists and that self-organising preferential flow paths can be exploited to deliver MICP reagents further into masonry repair zones without blocking the injection point.

4.2. Grouting with MICP

MICP grouting of the column can be considered a success as the loose marble pack was cemented into a single solid volume up to a depth of 150 mm from the inlet. The white $CaCO_3$ cement was visually indistinguishable from the original marble grains and formed a smooth surface on the inlet face of the column.

To prevent blocking of the inlet, it was necessary to remove the first five mm of marble grains after the fourth batch of MICP. In this experiment, blocking of the inlet is thought to have been enhanced by the small liquid volume in the flow distribution plate, located between the injection point and the marble pack. Flow velocities in this region were lower than inside the marble pack, leading to greater bacterial attachment on the inlet surface. Additionally, there was the potential for mixing of bacteria and cementing solution with precipitation occurring outside the marble pack then settling on top.

As shown by the X-CT results, precipitation was not uniform throughout the column: there was a gradient from inlet to outlet. This may be the result of a number of combined processes: 1) greater bacterial attachment – in line with filtration theory – leading to greater $CaCO_3$ precipitation at the inlet, 2) urea and $CaCl_2$ are consumed close to the inlet and become limiting factors for $CaCO_3$ precipitation further into the column, 3) bacteria are preferentially attaching to the previously precipitated $CaCO_3$ [36].

For real-world stone restoration with MICP grouting, careful consideration should be given to the method of injecting the
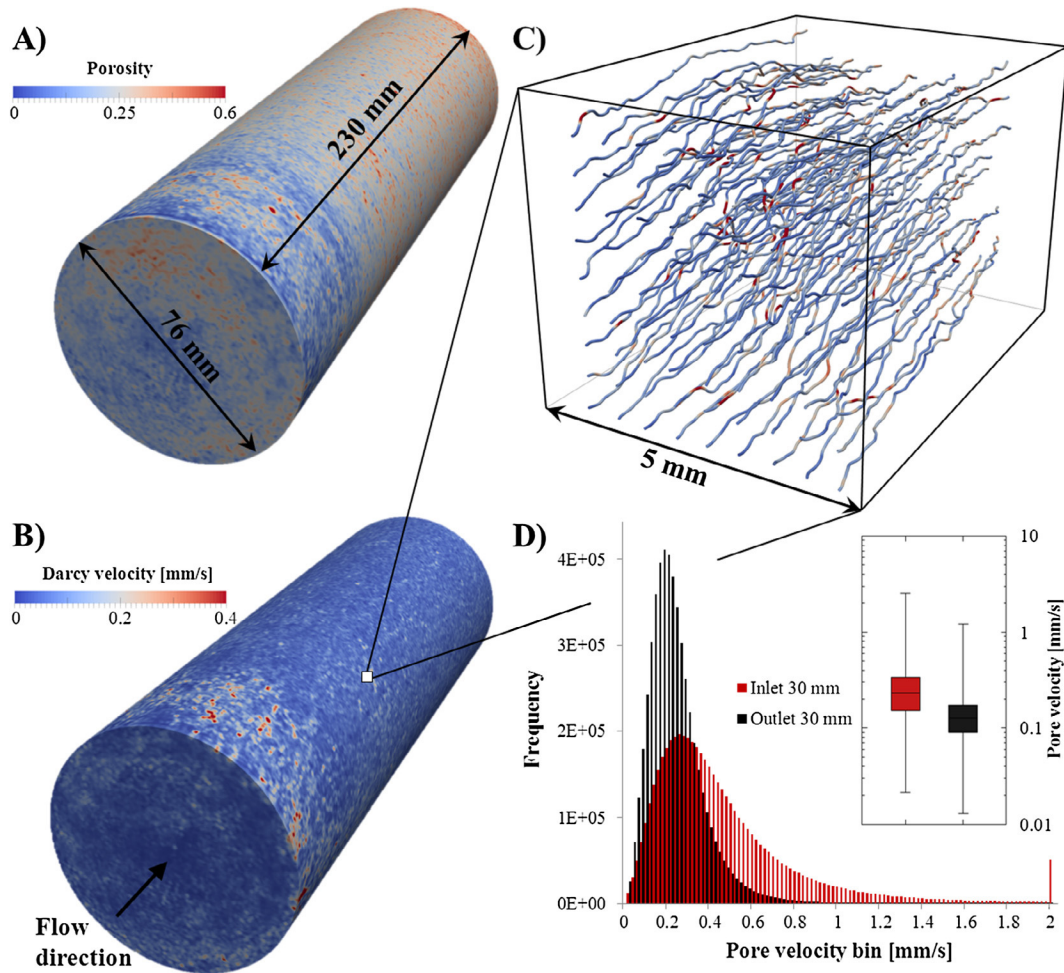
Fig. 10. A) Porosity distribution after six MICP batches determined from the X–CT scan. B) Modelled velocity distribution . C) Expanded view of model output showing flow paths (derived from the velocity vector field) and coloured by porosity. D) Histograms and boxplots of pore velocity for the first and last 30 mm of the modelled domain.
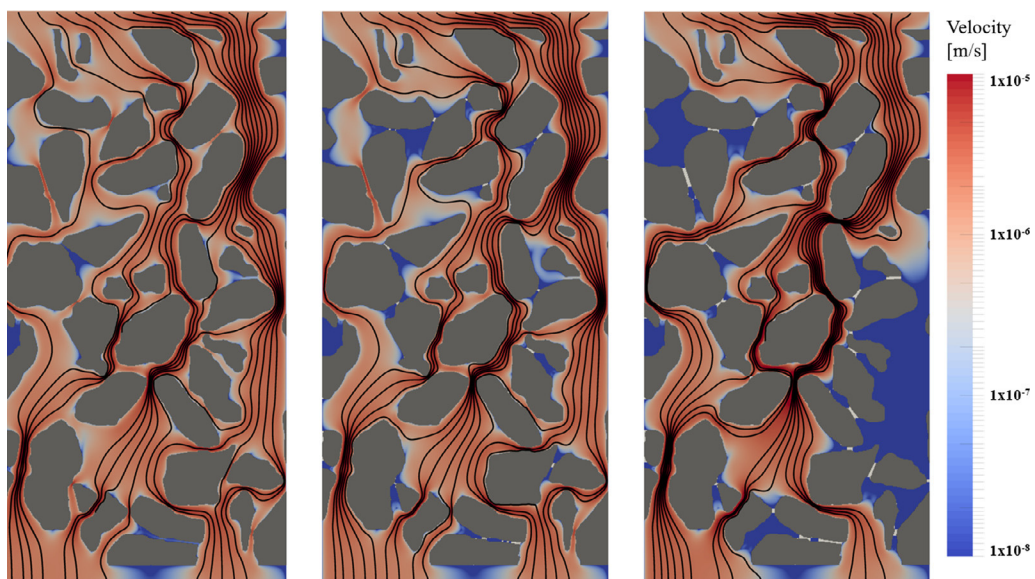

Fig. 11. Illustration of progressive CaCO$_3$ precipitation and the disconnection of pore bodies: flow through marble grains (shown in grey) calculated with the model presented in Section 3.1, black streamlines calculated with ParaView, and white 'CaCO$_3$ precipitate' manually inserted at grain contact points. Left: initial conditions, majority of pore space is connected. Middle: low level of CaCO$_3$ precipitate occupying 0.2% of the total initial pore space, small regions of pore space become disconnected. Right: moderate CaCO$_3$ precipitation occupying 0.7% of the total initial pore space, pore throats are closed off and large volumes of the pore space are disconnected despite the low volume of precipitate.

bacteria and cementing solution so as to limit the potential for mixing of solutions before they enter the porous media. If more uniform grout penetration is required over depths of greater than 150 mm, end-users may want to consider the following alterations to the injection strategy:

1. Inject at a higher flow rate to decrease bacterial attachment and distribute the bacteria deeper into cracks/porous media. Continuous fluid injection may be required throughout the treatment process to ensure these channels remain open.
2. Allow for a higher maximum injection pressure so that, as $CaCO_3$ precipitation progresses, there is no need to unblock the injection point.
3. If the technique were to be used in cracks with larger existing grains (e.g. at an earlier stage of structural weathering) reduced bacterial removal by straining would be expected, resulting in a more even distribution throughout the column.
4. For crack remediation with pre-packed filler material, the use of a narrower grain size distribution would create more porosity. Strength improvement from precipitation at grain contact points could therefore occur before permeability reduction limited the penetration of further MICP batches.

5. Conclusions

MICP treatment was carried out in a column filled with marble grains with the injection of six batches over six days. A white $CaCO_3$ precipitate was produced which matched the original marble colour and was sufficiently strong to cement the marble sand together from the inlet up to a depth of 150 mm into the column. This research shows that cracks in degraded marble of considerable size could be remediated with MICP by first packing them with marble grains and then precipitating carbonate cement.

X-ray CT revealed a gradient in $CaCO_3$ precipitation with greatest precipitation at the inlet. It is reasoned that this could be avoided by modification to the injection strategy. Prevention of re-agent mixing outside the marble grains, careful choice of marble grain size distribution, and tailored injection flow rates could deliver re-agents deeper into the media and take advantage of the formation of stable flow pathways to maximise seal uniformity. MICP is therefore a promising technique for the restoration of marble structures and monuments.

6. Conflict of interests

The authors declare no conflict of interests regarding the publication of this paper.

References

[1] M.J. Mosquera, J. Pozo, L. Esquivias, Stress during drying of two stone consolidants applied in monumental conservation, J. Sol-Gel Sci. Technol. 26 (2003) 1227–1231, https://doi.org/10.1023/A:1020776622689.
[2] P. Fermo, G. Cappelletti, N. Cozzi, G. Padeletti, S. Kaciulis, M. Brucale, M. Merlini, Hydrophobizing coatings for cultural heritage. A detailed study of resin/stone surface interaction, Appl. Phys. A Mater. Sci. Process. 116 (2014) 341–348, https://doi.org/10.1007/s00339-013-8127-z.
[3] Q. Liu, Y. Liu, K. Zeng, F. Yang, H. Zhu, Q. Liu, Advanced design of Chinese traditional materials for the conservation of historic stone buildings, J. Archaeol. Sci. 38 (2011) 1896–1900.
[4] P. Baglioni, D. Chelazzi, R. Giorgi, G. Poggi, Colloid and materials science for the conservation of cultural heritage: cleaning, consolidation, and deacidification, Langmuir 29 (2013) 5110–5122, https://doi.org/10.1021/la304456n.
[5] E. Boquet, A. Boronat, A. Ramos-Cormenzana, Production of calcite (calcium carbonate) crystals by soil bacteria is a general phenomenon, Nature 246 (1973) 527–529, https://doi.org/10.1038/246527a0.
[6] I.A. Bundeleva, L.S. Shirokova, P. Bénézeth, O.S. Pokrovsky, E.I. Kompantseva, S. Balor, Calcium carbonate precipitation by anoxygenic phototrophic bacteria, Chem. Geol. 291 (2012) 116–131, https://doi.org/10.1016/j.chemgeo.2011.10.003.
[7] C. Jimenez-Lopez, C. Rodriguez-Navarro, G. Piñar, F.J. Carrillo-Rosúa, M. Rodriguez-Gallego, M.T. Gonzalez-Muñoz, Consolidation of degraded ornamental porous limestone stone by calcium carbonate precipitation induced by the microbiota inhabiting the stone, Chemosphere 68 (2007) 1929–1936, https://doi.org/10.1016/j.chemosphere.2007.02.044.
[8] G. Le Métayer-Levrel, S. Castanier, G. Orial, J.F. Loubière, J.P. Perthuisot, Applications of bacterial carbonatogenesis to the protection and regeneration of limestones in buildings and historic patrimony, Sediment. Geol. 126 (1999) 25–34, https://doi.org/10.1016/S0037-0738(99)00029-9.
[9] C. Rodriguez-Navarro, M. Rodriguez-Gallego, K. Ben Chekroun, M.T. Gonzalez-Muñoz, Conservation of ornamental stone by Myxococcus xanthus-induced carbonate biomineralization conservation of ornamental stone by myxococcus xanthus-induced carbonate biomineralization, Appl. Environ. Microbiol. 69 (2003) 2182–2193, https://doi.org/10.1128/AEM.69.4.2182.
[10] W. De Muynck, K. Verbeken, N. De Belie, W. Verstraete, Influence of urea and calcium dosage on the effectiveness of bacterially induced carbonate precipitation on limestone, Ecol. Eng. 36 (2010) 99–111, https://doi.org/10.1016/j.ecoleng.2009.03.025.
[11] W. De Muynck, N. De Belie, W. Verstraete, Microbial carbonate precipitation in construction materials: a review, Ecol. Eng. 36 (2010) 118–136, https://doi.org/10.1016/j.ecoleng.2009.02.006.
[12] P.H. Li, W.J. Qu, Remediation of historic buildings and patrimony by bacterially induced mineralization, Adv. Mater. Res. 133–134 (2010) 1253–1258, https://doi.org/10.4028/www.scientific.net/AMR.133-134.1253.
[13] W.K. Zhu, T. Mu, Y.K. Zhang, T. Duan, X.G. Luo, Coating of microbially produced calcium carbonate onto stone materials, Sci. China Technol. Sci. 58 (2014) 266–272, https://doi.org/10.1007/s11431-014-5710-2.
[14] N. De Belie, W. De Muynck, Crack repair in concrete using biodeposition, in: M.G. Alexander, H.-D. Beushausen, F. Dehn, P. Moyo (Eds.), Proc. 2nd Int. Conf. Concr. Repair, Rehabil. Retrofit, CRC Press, Cape Town, South Africa, 2008, pp. 291–292, https://doi.org/10.1201/9781439828403.ch107.
[15] S.K. Ramachandran, V. Ramakrishnan, S.S. Bang, Remediation of concrete using micro-organisms, ACI Mater. J. 98 (2001) 3–9, https://doi.org/10.14359/10154.
[16] J.L. Day, V. Ramakrishnan, S.S. Bang, Microbiologically induced sealant for concrete crack remediation, in: Proc. 16th Eng. Mech. Conf., Seattle, 2003.
[17] A.J. Phillips, E. Lauchnor, J.J. Eldring, R. Esposito, A.C. Mitchell, R. Gerlach, A.B. Cunningham, L.H. Spangler, Potential CO_2 leakage reduction through biofilm-induced calcium carbonate precipitation, Environ. Sci. Technol. 47 (2013) 142–149, https://doi.org/10.1021/es301294q.
[18] M.O. Cuthbert, L.A. McMillan, S. Handley-Sidhu, M.S. Riley, D.J. Tobler, V.R. Phoenix, A field and modeling study of fractured rock permeability reduction using microbially induced calcite precipitation, Environ. Sci. Technol. 47 (2013) 13637–13643, https://doi.org/10.1021/es402601g.
[19] L. Zhong, M.R. Islam, A new microbial plugging process and its impact on fracture remediation, Soc. Pet. Eng. (1995) 703–715.
[20] J.M. Minto, E. MacLachlan, G. El Mountassir, R.J. Lunn, Rock fracture grouting with microbially induced carbonate precipitation, Water Resour. Res. 52 (2016) 8827–8844, https://doi.org/10.1002/2016WR018884.
[21] G. Orial, T. Vieweger, J.F. Loubiere, Les Mortiers Biologiques: une Solution Pour la Conservation de la Sculpture Monumentale en Pierre, New York, NY Art Biol. Conserv. Metrop. Museum (2002).
[22] Q. Tan, H. Guo, X. Cheng, The remediation of damaged stone by microbially induced carbonate precipitation, in: 4th Hist. Mortars Conf., Santorini, Greece, 2016.
[23] V.S. Whiffin, Microbial $CaCO_3$ precipitation for the production of biocement, Murdoch University, 2004.
[24] A.C. Mitchell, F.G. Ferris, The coprecipitation of Sr into calcite precipitates induced by bacterial ureolysis in artificial groundwater: Temperature and kinetic dependence, Geochim. Cosmochim. Acta. 69 (2005) 4199–4210, https://doi.org/10.1016/j.gca.2005.03.014.
[25] L. Cheng, R. Cord-Ruwisch, In situ soil cementation with ureolytic bacteria by surface percolation, Ecol. Eng. 42 (2012) 64–72, https://doi.org/10.1016/j.ecoleng.2012.01.013.
[26] L. Cheng, R. Cord-Ruwisch, Upscaling effects of soil improvement by microbially induced calcite precipitation by surface percolation, Geomicrobiol. J. 31 (2014) 396–406, https://doi.org/10.1080/01490451.2013.836579.
[27] L.A. van Paassen, M.P. Harkes, G.A. Van Zwieten, W.H. van der Zon, W.R.L. Van Der Star, M.C.M.M. van Loosdrecht, Scale up of biogrout: A biological ground reinforcement method, Proc. 17th Int. Conf. Soil Mech. Geotech. Eng. Acad. Pract Geotech. Eng. 3 (2009) 2328–2333, https://doi.org/10.3233/978-1-60750-031-5-2328.

[28] V.S. Whiffin, L.A. van Paassen, M.P. Harkes, Microbial carbonate precipitation as a soil improvement technique, Geomicrobiol. J. 24 (2007) 417–423, https://doi.org/10.1080/01490450701436505.

[29] G. Tang, M.A. Mayes, J.C. Parker, P.M. Jardine, CXTFIT/excel–A modular adaptable code for parameter estimation, sensitivity analysis and uncertainty analysis for laboratory or field tracer experiments, Comput. Geosci. 36 (2010) 1200–1209, https://doi.org/10.1016/j.cageo.2010.01.013.

[30] N. Toride, F.J. Leij, M.T.T. van Genuchten, The CXTFIT Code for Estimating Transport Parameters from Laboratory of Field Tracer Experiments, Version 2.1, Research Report No. 137, Riverside, California, 1999.

[31] C. Soulaine, H.A. Tchelepi, Micro-continuum approach for pore-scale simulation of subsurface processes, Transp. Porous Media. 113 (2016) 431–456, https://doi.org/10.1007/s11242-016-0701-3.

[32] J. Schindelin, C.T. Rueden, M.C. Hiner, K.W. Eliceiri, The imageJ ecosystem: an open platform for biomedical image analysis, Mol. Reprod. Dev. 82 (2015) 518–529, https://doi.org/10.1002/mrd.22489.

[33] M.H. Krause, J.-C. Perrin, S.M. Benson, Modeling permeability distributions in a sandstone core for history matching coreflood experiments, SPE Int. Conf. CO_2 Captrue Storage Util. 2009 (2011) 768–777, https://doi.org/10.2118/126340-MS.

[34] J.M. Minto, F.F.F. Hingerl, S.M. Benson, R.J. Lunn, X-ray CT and multiphase flow characterization of a "bio-grouted" sandstone core: the effect of dissolution on seal longevity, Int. J. Greenh. Gas Control. 64 (2017) 152–162, https://doi.org/10.1016/j.ijggc.2017.07.007.

[35] G. El Mountassir, R.J. Lunn, H. Moir, E. MacLachlan, Hydrodynamic coupling in microbially mediated fracture mineralization: formation of self-organized groundwater flow channels, Water Resour. Res. 50 (2014) 1–16, https://doi.org/10.1002/2013WR013578.

[36] D.J. Tobler, E. Maclachlan, V.R. Phoenix, Microbially mediated plugging of porous media and the impact of differing injection strategies, Ecol. Eng. 42 (2012) 270–278, https://doi.org/10.1016/j.ecoleng.2012.02.027.